

Isotropy of three-dimensional quantum lattice Boltzmann schemes

P. J. Dellar^{*} and D. Lapitski

OClAM, Mathematical Institute, 24–29 St Giles', Oxford OX1 3LB, United Kingdom

S. Palpacelli

Numidia Società a responsabilità limitata, via Berna 31, I-00144 Roma, Italy

S. Succi

Istituto Applicazioni del Calcolo, Consiglio Nazionale delle Ricerche, via dei Taurini 19, I-00185 Roma, Italy

(Received 8 December 2010; published 7 April 2011)

Numerical simulations with previous formulations of the quantum lattice Boltzmann (QLB) scheme in three spatial dimensions showed significant lack of isotropy. In two or more spatial dimensions the QLB approach relies upon operator splitting to decompose the time evolution into a sequence of applications of the one-dimensional QLB scheme along coordinate axes. Each application must be accompanied by a rotation of the wave function into a basis of chiral eigenstates aligned along the relevant axis. The previously observed lack of isotropy was due to an inconsistency in the application of these rotations. Once this inconsistency is removed, the QLB scheme is shown to exhibit isotropic behavior to within a numerical error that scales approximately linearly with the lattice spacing. This establishes the viability of the QLB approach in two and three spatial dimensions.

DOI: [10.1103/PhysRevE.83.046706](https://doi.org/10.1103/PhysRevE.83.046706)

PACS number(s): 02.70.-c, 03.65.-w

I. INTRODUCTION

The lattice Boltzmann approach has developed into a very attractive computational tool for simulating fluid dynamics, especially in complex geometries, and on modern parallel computer architectures [1–5]. These advantages follow from solving the Navier-Stokes equations not directly, but recovering them instead as the equations that describe slowly varying solutions of a discrete Boltzmann equation. The latter is a linear, constant coefficient hyperbolic system that is readily discretized by integrating along characteristics. All nonlinearity is confined to algebraic terms that are local to each grid point, and model collisions between particles.

In developing quantum lattice Boltzmann (QLB) methods [6–9] we aim to exploit these advantages to develop algorithms for simulating quantum systems described by the Schrödinger equation. Again, we do not attempt to simulate the Schrödinger equation directly, but instead recover it as the limiting equation that describes slowly varying solutions of the Dirac equation. The Dirac equation offers a quantum-mechanical description of a particle that is compatible with special relativity [10]. Like the discrete Boltzmann equation, the Dirac equation is a linear, constant coefficient hyperbolic system, with algebraic source terms. Both equations contain only single partial derivatives with respect to time and space. By contrast, the Navier-Stokes and Schrödinger equations both contain one derivative with respect to time, but two derivatives with respect to space. This asymmetry between space and time renders the Schrödinger equation incompatible with special relativity, and also incompatible with being discretized by integration along characteristics.

The discrete Boltzmann and Dirac equations are both linear, symmetric hyperbolic systems in the sense of Friedrichs [11]. These properties guarantee the existence of weak solutions to initial value problems [12]. However, the three-dimensional

discrete Boltzmann equation, Eq. (8) below, is very unusual in having characteristic curves. The most one may normally expect is for the characteristic surfaces, the surfaces along which discontinuities in solutions propagate, to be three-dimensional surfaces within the four-dimensional (x, t) space [13]. In more algebraic language, the flux Jacobian matrices for the Dirac equation are real and symmetric when the Dirac equation is written in Majorana form, as in Eq. (6) below. However, these matrices are not diagonal, and they cannot be simultaneously diagonalized by any change of basis. Therefore the construction of numerical solutions to the Dirac equation cannot be reduced to integrating along characteristic curves. The ultimate source of this difficulty lies in the Dirac equation's description of particles with spin, and the noncommuting properties of the Pauli spin matrices [10].

A number of quantum cellular automata (QCA) have been formulated [14–19], following Feynman's checkerboard representation of solutions to the one-dimensional Dirac equation in terms of particles executing random walks in a discrete space-time [20]. In particular, quantum lattice gas cellular automata (QLGCA) [15–19] are a specific class of QCA that adopt the two-step "stream-collide" rule typical of lattice gas cellular automata from hydrodynamics [21,22]. All these quantum automata deal with continuous complex scalar fields instead of the Boolean variables of classical automata that take just the values 0 or 1. Instead, QLGCA propagate *quantum* bits (qubits) that correspond to arbitrary superpositions of the two basic quantum states $|0\rangle$ and $|1\rangle$. More precisely, a quantum bit may be written as $q = c_0|0\rangle + c_1|1\rangle$, where c_0 and c_1 are complex scalars, such that $p_0 = |c_0|^2$ and $p_1 = |c_1|^2 = 1 - p_0$ give the probability for the quantum particle to be in state $|0\rangle$ (empty) or $|1\rangle$ (occupied), respectively. Qubits exhibit a one-to-one correspondence with spin-1/2 fermions whose up-down components propagate along opposite directions, say $\pm z$, in physical space. As QLGCA support arbitrary superpositions of the Boolean states, they are formally equivalent to QLB schemes [16,18]. For

*dellar@maths.ox.ac.uk

example, a QCA studied by Meyer is unitarily equivalent to the one-dimensional QLB scheme [15]. In this respect, QLGCA and QLB can both be regarded as computational “engines” that propagate and collide qubits in compliance with the rule of relativistic quantum mechanics. By contrast, a classical lattice Boltzmann scheme is obtained by coarse graining the microscopic Boolean configurations in a classical LGCA, via either ensemble or space-time averaging. A similar bottom-up relation has long been advocated in the quantum context by ’t Hooft [23,24], who has proposed that quantum-mechanical wave dynamics may emerge as the continuum limit of an underlying deterministic local and reversible cellular automaton. Besides reviving the time-honored “hidden variable” picture in a modern guise, ’t Hooft’s approach offers tantalizing but still highly speculative connections with quantum gravity.

Turning to more immediate applications, nonlinear extensions of the QLB scheme may be used to simulate the Gross-Pitaevskii equation that describes Bose-Einstein condensates [9,25]. The underlying capability of the QLB schemes for solving the Dirac equation [26] suggests further applications to simulating Bose-Einstein condensates in honeycomb optical lattices [27]. The motion of charge carriers in graphene, the two-dimensional hexagonal lattice form of carbon, is also described by the Dirac equation [28–31], with the Fermi velocity $v_F \approx 10^6 \text{ m s}^{-1}$ acting as the effective speed of light. We expect that the two-dimensional QLB algorithm will find a useful role in simulating experiments with graphene.

II. DIRAC EQUATION

The Dirac equation offers a quantum-mechanical description of an electron that is compatible with special relativity. The form we take for our starting point is

$$(\partial_t + c\boldsymbol{\alpha} \cdot \nabla)\Psi = -i\omega_c\beta\Psi + ig\Psi, \quad (1)$$

where c is the light speed, \hbar is the reduced Planck’s constant, and $\omega_c = mc^2/\hbar$ is the Compton frequency for a particle of mass m . The wave function Ψ is a column vector with four components, β is a 4×4 matrix, and $\boldsymbol{\alpha} = (\alpha^x, \alpha^y, \alpha^z)$ is a collection of three 4×4 matrices, so that $\boldsymbol{\alpha} \cdot \nabla = \alpha^x\partial_x + \alpha^y\partial_y + \alpha^z\partial_z$. The last term couples the wave function to an applied scalar potential V via the coefficient $g = qV/\hbar$, where q is the modulus of an electron’s charge.

In the standard representation [10] of the Dirac equation, the α and β matrices are

$$\begin{aligned} \alpha^x &= \begin{pmatrix} 0 & 0 & 0 & 1 \\ 0 & 0 & 1 & 0 \\ 0 & 1 & 0 & 0 \\ 1 & 0 & 0 & 0 \end{pmatrix}, & \alpha^y &= \begin{pmatrix} 0 & 0 & 0 & -i \\ 0 & 0 & i & 0 \\ 0 & -i & 0 & 0 \\ i & 0 & 0 & 0 \end{pmatrix}, \\ \alpha^z &= \begin{pmatrix} 0 & 0 & 1 & 0 \\ 0 & 0 & 0 & -1 \\ 1 & 0 & 0 & 0 \\ 0 & -1 & 0 & 0 \end{pmatrix}, & \beta &= \begin{pmatrix} 1 & 0 & 0 & 0 \\ 0 & 1 & 0 & 0 \\ 0 & 0 & -1 & 0 \\ 0 & 0 & 0 & -1 \end{pmatrix}. \end{aligned} \quad (2)$$

The three α matrices may be written in block form as

$$\alpha^i = \begin{pmatrix} 0 & \sigma^i \\ \sigma^i & 0 \end{pmatrix}, \quad (3)$$

where the off-diagonal blocks are the three Pauli spin matrices [10]

$$\sigma^x = \begin{pmatrix} 0 & 1 \\ 1 & 0 \end{pmatrix}, \quad \sigma^y = \begin{pmatrix} 0 & -i \\ i & 0 \end{pmatrix}, \quad \sigma^z = \begin{pmatrix} 1 & 0 \\ 0 & -1 \end{pmatrix}. \quad (4)$$

These matrices satisfy the well-known commutation relations

$$\sigma^i\sigma^j - \sigma^j\sigma^i = 2i\epsilon_{ijk}\sigma^k, \quad (5)$$

where ϵ_{ijk} is the alternating Levi-Civita tensor. The essential fact that underlies this paper is that the spin matrices do not commute. There is thus no basis in which all three matrices are simultaneously diagonal, and the same holds for the 4×4 matrices $\alpha^x, \alpha^y, \alpha^z$ built from the spin matrices.

For our purposes it is convenient to transform the standard form of the Dirac equation into the Majorana form [10],

$$[\partial_t + c(-\alpha^x\partial_x + \beta\partial_y - \alpha^z\partial_z) + i\omega_c\alpha^y - igI]\psi = 0, \quad (6)$$

by multiplying the standard form on the left and on the right by the involution matrix $U = 2^{-1/2}(\alpha^y + \beta)$. The transformed wave function in Eq. (6) is $\psi = U\Psi$. The Majorana transformation interchanges the roles of the α^y and β matrices between Eqs. (1) and (6). The resulting equation (6) has the desirable property that the three matrices $\alpha^x, \beta, \alpha^z$ multiplying the spatial derivatives $\partial_x, \partial_y, \partial_z$ are all real. The matrix α^y with complex coefficients has been moved into the algebraic terms.

The quantum lattice Boltzmann (QLB) approach is based on the structural similarity between Eq. (6) and the discrete Boltzmann equation with a matrix collision operator,

$$(\partial_t + \boldsymbol{\xi}_i \cdot \nabla)f_i = \sum_{j=0}^n \Omega_{ij}(f_j - f_j^{(0)}), \quad (7)$$

for $i = 0, \dots, n$. In particular, Eqs. (6) and (7) each contain only first derivatives in space and time. The distribution functions f_i are analogous to the four components of the wave function ψ , the set of discrete velocities $\boldsymbol{\xi}_i$ is analogous to the set of streaming matrices $\alpha^x, \beta, \alpha^z$. The collision matrix Ω_{ij} is analogous to the matrix α^y in the Dirac equation. The first hydrodynamic lattice Boltzmann schemes contained collision matrices derived from linearizing lattice gas collision operators [32,33]. These were later replaced by scattering matrices constructed from a known, rotationally symmetric set of eigenvectors [5,34]. More recent work uses collision matrices defined through their action on a basis of moments of the distribution functions [35–37].

Rewriting Eq. (7) in an explicit matrix form like Eqs. (1) and (6) gives

$$\begin{aligned} &\left[\partial_t + \begin{pmatrix} \xi_{0x} & 0 & \cdots & 0 \\ 0 & \xi_{1x} & \cdots & 0 \\ \vdots & \vdots & \ddots & \vdots \\ 0 & 0 & \cdots & \xi_{nx} \end{pmatrix} \partial_x + \begin{pmatrix} \xi_{0y} & 0 & \cdots & 0 \\ 0 & \xi_{1y} & \cdots & 0 \\ \vdots & \vdots & \ddots & \vdots \\ 0 & 0 & \cdots & \xi_{ny} \end{pmatrix} \partial_y \right. \\ &\quad \left. + \begin{pmatrix} \xi_{0z} & 0 & \cdots & 0 \\ 0 & \xi_{1z} & \cdots & 0 \\ \vdots & \vdots & \ddots & \vdots \\ 0 & 0 & \cdots & \xi_{nz} \end{pmatrix} \partial_z \right] \begin{pmatrix} f_0 \\ f_1 \\ \vdots \\ f_n \end{pmatrix} = \boldsymbol{\Omega} \begin{pmatrix} f_0 - f_0^{(0)} \\ f_1 - f_1^{(0)} \\ \vdots \\ f_n - f_n^{(0)} \end{pmatrix}. \end{aligned} \quad (8)$$

Each of the matrices multiplying ∂_x , ∂_y , ∂_z is diagonal, so a formal solution to Eq. (8) is readily obtained by integrating along the characteristics defined by the vectors ξ_i , as in Ref. [38]. He and Luo [39,40] gave another formal solution based on removing the algebraic term with an integrating factor before integrating along characteristics. Neither approach can be applied to the Dirac equation, because the three streaming matrices cannot be simultaneously diagonalized in either the standard or the Majorana forms. Instead, we fall back on the technique of operator splitting to approximate solutions to Eq. (6) by evolving the solution in one spatial dimension at a time.

III. ONE-DIMENSIONAL QUANTUM LATTICE BOLTZMANN MODEL

The y streaming matrix β is diagonal in the Majorana form (6) of the three-dimensional Dirac equation. However, the other streaming matrices may be diagonalized by applying unitary transformations. The matrix $-\alpha^z$ may be diagonalized as

$$Z^{-1}(-\alpha^z)Z = \begin{pmatrix} 1 & 0 & 0 & 0 \\ 0 & 1 & 0 & 0 \\ 0 & 0 & -1 & 0 \\ 0 & 0 & 0 & -1 \end{pmatrix}, \quad (9)$$

using the unitary matrix

$$Z = \frac{1}{\sqrt{2}} \begin{pmatrix} 0 & -1 & 0 & 1 \\ 1 & 0 & -1 & 0 \\ 0 & 1 & 0 & 1 \\ 1 & 0 & 1 & 0 \end{pmatrix}. \quad (10)$$

Applying this to Eq. (6), we multiply on the left by Z^{-1} to obtain

$$Z^{-1}[\partial_t + c(-\alpha^x \partial_x + \beta \partial_y - \alpha^z \partial_z) + i\omega_c \alpha^y - igI]\psi = 0, \quad (11)$$

and insert a factor of $ZZ^{-1} = I$,

$$Z^{-1}[\partial_t + c(-\alpha^x \partial_x + \beta \partial_y - \alpha^z \partial_z) + i\omega_c \alpha^y - igI]Z Z^{-1}\psi = 0. \quad (12)$$

In this way the streaming matrix along z is diagonalized,

$$[\partial_t + cZ^{-1}(-\alpha^z)Z\partial_z + Z^{-1}(-c\alpha^x \partial_x + c\beta \partial_y + i\omega_c \alpha^y - igI)Z]Z^{-1}\psi = 0, \quad (13)$$

while the rotated collision matrices are

$$\begin{aligned} -Z^{-1}(i\omega_c \alpha^y - igI)Z &= \omega_c \beta \alpha^x + igI \\ &= \begin{pmatrix} ig & 0 & 0 & \omega_c \\ 0 & ig & \omega_c & 0 \\ 0 & -\omega_c & ig & 0 \\ -\omega_c & 0 & 0 & ig \end{pmatrix}. \end{aligned} \quad (14)$$

We insert a minus sign throughout because the rotated collision matrices appear on the right hand sides of (15) and (16). Neglecting any dependence of ψ on the x and y coordinates, the combination Eqs. (13) and (14) may be written as a pair of

one-dimensional Dirac equations,

$$\begin{aligned} \partial_t u_{1,2} + c\partial_z u_{1,2} &= \omega_c d_{2,1} + igu_{1,2}, \\ \partial_t d_{1,2} - c\partial_z d_{1,2} &= -\omega_c u_{2,1} + igd_{1,2}, \end{aligned} \quad (15)$$

for the variables (u_1, d_2) and (u_2, d_1) that make up the rotated wave function $Z^{-1}\psi = (u_1, u_2, d_1, d_2)^T$. The components u and d propagate up and down the z axis, respectively, and the subscripts indicate the spin up (1) and spin down (2) states, respectively. The variables $u_{1,2}$ and $d_{1,2}$ are thus the Riemann invariants [13] of the differential operator for streaming along z .

As observed in Ref. [6], the system (15) may be treated as a Boltzmann equation for a pair of complex distribution functions $u_{1,2}$ and $d_{1,2}$. Equation (15) may thus be discretized by following the same approach that leads from the discrete Boltzmann equation (7) to a lattice Boltzmann scheme [38].

The left hand sides of Eq. (15) are derivatives along the characteristics given by the light cones $(z \pm cs, t + s)$ parametrized by s . Integrating along these characteristics therefore gives exactly the difference in variable $u_{1,2}$ or $d_{1,2}$ between the two ends of the characteristic. The right hand side of Eq. (15) is discretized using the trapezoidal rule, which involves the average of the values at time t and position z and time $t + \Delta t$ and position $z \pm \Delta z$. We evaluate $u_{1,2}$ at $z + \Delta z$ and $d_{1,2}$ at $z - \Delta z$, since these are the points appearing in the discretization of the left hand side. The resulting system of algebraic equations is

$$\begin{aligned} \widehat{u}_{1,2} - u_{1,2} &= \frac{1}{2}\tilde{m}(d_{2,1} + \widehat{d}_{2,1}) + \frac{1}{2}i\tilde{g}(u_{1,2} + \widehat{u}_{1,2}), \\ \widehat{d}_{1,2} - d_{1,2} &= -\frac{1}{2}\tilde{m}(u_{2,1} + \widehat{u}_{2,1}) + \frac{1}{2}i\tilde{g}(d_{1,2} + \widehat{d}_{1,2}), \end{aligned} \quad (16)$$

where a superscript hat ($\widehat{\cdot}$) indicates that a variable is evaluated somewhere other than (z, t) ,

$$\begin{aligned} \widehat{u}_{1,2} &= u_{1,2}(z + \Delta z, t + \Delta t), & u_{1,2} &= u_{1,2}(z, t), \\ \widehat{d}_{1,2} &= d_{1,2}(z - \Delta z, t + \Delta t), & d_{1,2} &= d_{1,2}(z, t). \end{aligned} \quad (17)$$

The dimensionless Compton frequency is $\tilde{m} = \omega_c \Delta t$, and the dimensionless scalar potential is $\tilde{g} = g(z, t) \Delta t$.

The pair of equations (16) may be solved algebraically to obtain explicit formulas for $\widehat{u}_{1,2}$ and $\widehat{d}_{1,2}$,

$$\begin{aligned} \widehat{u}_{1,2} &= au_{1,2} + bd_{2,1}, \\ \widehat{d}_{1,2} &= ad_{1,2} - bu_{2,1}, \end{aligned} \quad (18)$$

where the coefficients a and b are

$$a = \frac{1 - \Omega/4}{1 + \Omega/4 - i\tilde{g}}, \quad b = \frac{\tilde{m}}{1 + \Omega/4 - i\tilde{g}}, \quad \Omega = \tilde{m}^2 - \tilde{g}^2.$$

These coefficients satisfy $|a|^2 + |b|^2 = 1$, so the right hand side of Eq. (18) corresponds to multiplying the rotated wave function $Z^{-1}\psi = (u_1, u_2, d_1, d_2)^T$ by the unitary collision matrix,

$$Q = \begin{pmatrix} a & 0 & 0 & b \\ 0 & a & b & 0 \\ 0 & -b & a & 0 \\ -b & 0 & 0 & a \end{pmatrix}. \quad (19)$$

The streaming step propagates $u_{1,2}$ upward, and $d_{1,2}$ downward, along the light cones given by $\Delta z = \pm c\Delta t$. This is also a unitary operation, so the overall QLB scheme evolves the discrete wave function through a sequence of unitary operations.

IV. A THREE-DIMENSIONAL SCHEME VIA OPERATOR SPLITTING

We use operator splitting to decompose the three-dimensional Dirac equation into the sum of three one-dimensional equations, each involving spatial derivatives along a single direction. We thus write the Majorana form of the Dirac equation as

$$\begin{aligned} & \{\partial_t + [c(-\alpha^x)\partial_x + \frac{1}{3}i(\omega_c\alpha^y + gI)] \\ & + [c\beta\partial_y + \frac{1}{3}i(\omega_c\alpha^y + gI)] \\ & + [c(-\alpha^z)\partial_z + \frac{1}{3}i(\omega_c\alpha^y + gI)]\}\psi = 0, \end{aligned} \quad (20)$$

where each term $[\dots]$ is an operator for streaming in one direction and collision. We split the collision term into three equal pieces, and include one piece in each bracketed term to match the form of the one-dimensional Dirac equation of the last section.

We use operator splitting to approximate the evolution over a time step Δt by decomposing Eq. (20) into three separate equations. Using the notation $\exp\{\Delta t[\dots]\}\psi_0$ for the solution of the linear evolution equation $\partial_t\psi = [\dots]\psi$ with initial condition ψ_0 over a time interval Δt , our operator splitting corresponds to computing

$$\psi' = \exp\{\Delta t[c(-\alpha^x)\partial_x + \frac{1}{3}i(\omega_c\alpha^y + gI)]\}\psi(t), \quad (21a)$$

$$\psi'' = \exp\{\Delta t[c\beta\partial_y + \frac{1}{3}i(\omega_c\alpha^y + gI)]\}\psi', \quad (21b)$$

$$\psi(t + \Delta t) = \exp\{\Delta t[c(-\alpha^z)\partial_z + \frac{1}{3}i(\omega_c\alpha^y + gI)]\}\psi''. \quad (21c)$$

The three operators do not commute, so we incur an $\mathcal{O}(\Delta t^2)$ splitting error by using this product of exponentials to approximate the exponential of the sum of the three operators.

Each of the three stages in Eqs. (21) denoting evolution by a time step Δt is accomplished by rotating ψ to diagonalize the relevant streaming matrix, taking one time step of the existing one-dimensional QLB scheme described above, and rotating ψ back to its original basis. Our algorithm is thus composed of the following steps

- (i) Rotate ψ with X^{-1} , collide with $X^{-1}\widehat{Q}X$, stream along x , rotate back with X .
- (ii) Rotate ψ with Y^{-1} , collide with $Y^{-1}\widehat{Q}Y$, stream along y , rotate back with Y .
- (iii) Rotate ψ with Z^{-1} , collide with $Z^{-1}\widehat{Q}Z$, stream along z , rotate back with Z .

We have written the algorithm like this to emphasize the symmetry between the three steps, but the matrix for streaming

along y is already diagonal in the Majorana form, so $Y = I$ is the identity matrix. The matrix X is

$$X = \frac{1}{\sqrt{2}} \begin{pmatrix} -1 & 0 & 1 & 0 \\ 0 & 1 & 0 & -1 \\ 1 & 0 & 1 & 0 \\ 0 & 1 & 0 & 1 \end{pmatrix}, \quad (22)$$

and the Z matrix is given in Eq. (10) above.

We have chosen to split the collision term into three parts, each of which is combined with one of the streaming steps. The collision matrix thus coincides, up to a unitary transformation, with the collision matrix for the one-dimensional QLB scheme with a time step of $\frac{1}{3}\Delta t$ (see Ref. [8]). In particular, \widehat{Q} is given by

$$\widehat{Q} = \begin{pmatrix} \widehat{a} & 0 & 0 & -\widehat{b} \\ 0 & \widehat{a} & \widehat{b} & 0 \\ 0 & -\widehat{b} & \widehat{a} & 0 \\ \widehat{b} & 0 & 0 & \widehat{a} \end{pmatrix}, \quad (23)$$

where the coefficients

$$\widehat{a} = \frac{1 - \Omega_3/4}{1 + \Omega_3/4 - i\tilde{g}_3}, \quad \widehat{b} = \frac{\tilde{m}_3}{1 + \Omega_3/4 - i\tilde{g}_3},$$

are written in terms of the rescaled dimensionless Compton and potential frequencies,

$$\Omega_3 = \tilde{m}_3^2 - \tilde{g}_3^2, \quad \tilde{m}_3 = \frac{1}{3}\omega_c\Delta t, \quad \tilde{g}_3 = \frac{1}{3}g\Delta t.$$

The pattern of + and – signs in the \widehat{b} terms on the off-diagonal of \widehat{Q} follows the same pattern as the α^y matrix. The rotated matrices $X^{-1}\widehat{Q}X$ and $Z^{-1}\widehat{Q}Z$ have the same sign pattern as Q , but \widehat{Q} itself does not.

V. NUMERICAL RESULTS

To verify the isotropic nature of the scheme we choose initial conditions in which the positive energy, spin-up component ϕ_1^+ is a spherically symmetric Gaussian wave packet with spread Δ_0 ,

$$\phi_1^+(x, y, z, t) = (2\pi\Delta_0^2)^{-3/4} \exp\left(-\frac{x^2 + y^2 + z^2}{4\Delta_0^2}\right). \quad (24)$$

The other three components ϕ_2^+ and $\phi_{1,2}^-$ are initially set to zero. As a first measure of isotropy, we study the temporal evolution of the standard deviations of $|\phi_1^+|^2$ in each of the three coordinate directions. These quantities are defined by

$$\Delta_x = \left(\int x^2 |\phi_1^+|^2 dV \right)^{1/2} / \left(\int |\phi_1^+|^2 dV \right)^{1/2}, \quad (25)$$

and similarly for Δ_y and Δ_z . We calculate discrete approximations to these integrals using the trapezoidal rule,

$$\Delta_x = \left(\sum_{i,j,k} x_i^2 |\phi_1^+|^2 dV \right)^{1/2} / \left(\sum_{i,j,k} |\phi_1^+|^2 dV \right)^{1/2}. \quad (26)$$

Although usually only second-order accurate, the trapezoidal rule becomes exponentially accurate when the sums are taken

over grids of equally spaced points in a domain with periodic boundary conditions [41].

A. Free particle

The solution of the Schrödinger equation for a free particle ($V = 0$) with initial conditions given by Eq. (24) is

$$\phi(x, y, z, t) = \frac{\exp\left(-\frac{x^2+y^2+z^2}{4\Delta_0^2+2i\hbar t/m}\right)}{(\sqrt{2\pi}[\Delta_0 + i\hbar t/(2m\Delta)])^{3/2}}. \quad (27)$$

The three spreads are thus given by

$$\Delta_\alpha(t) = \left(\Delta_0^2 + \frac{\hbar^2 t^2}{4m^2 \Delta_0^2}\right)^{1/2}, \quad (28)$$

for $\alpha = x, y, z$. Figure 1 shows the measured spreads for a free particle with $m = 0.35$ and $\Delta_0 = 14$ in a cube with side length $\ell = 100$ discretized using 128^3 points. We use natural units in which $c = 1$ and $\hbar = 1$. The three spreads Δ_x , Δ_y , Δ_z are in good agreement with each other, and follow the general trend of the Schrödinger solution as given by Eq. (28). However, the computed spreads deviate from the Schrödinger solution through superimposed small amplitude oscillations at the Compton frequency. These oscillations are intrinsic to the Dirac equation, and are due to relativistic effects associated with a particle of finite mass. In a forthcoming publication we show that the QLB solution is a consistent numerical solution of the original Dirac equation [26].

Figure 2 shows the deviation from isotropy as measured by the mean difference between the three spreads,

$$\tilde{\Delta} = \frac{1}{3}(|\Delta_x - \Delta_y| + |\Delta_x - \Delta_z| + |\Delta_y - \Delta_z|),$$

for three different computational grids with 128^3 , 256^3 , 512^3 , and 1024^3 points. As shown, $\tilde{\Delta}$ tends to decrease under grid

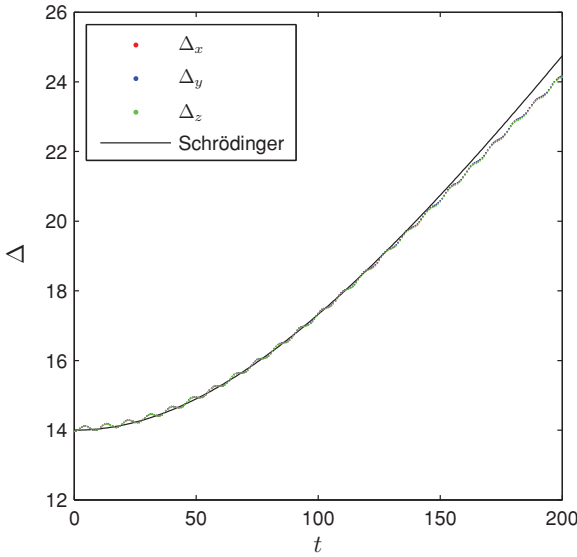


FIG. 1. (Color online) Dispersion of a wave packet with initial spread $\Delta_0 = 14$, particle mass $m = 0.35$, and no potential in a cube with side length $\ell = 100$ and a computational grid with 128^3 points. The three computed spreads Δ_x , Δ_y , Δ_z collapse onto a single curve, which differs by a superimposed high frequency oscillation from the Schrödinger solution (28) (smooth curve).

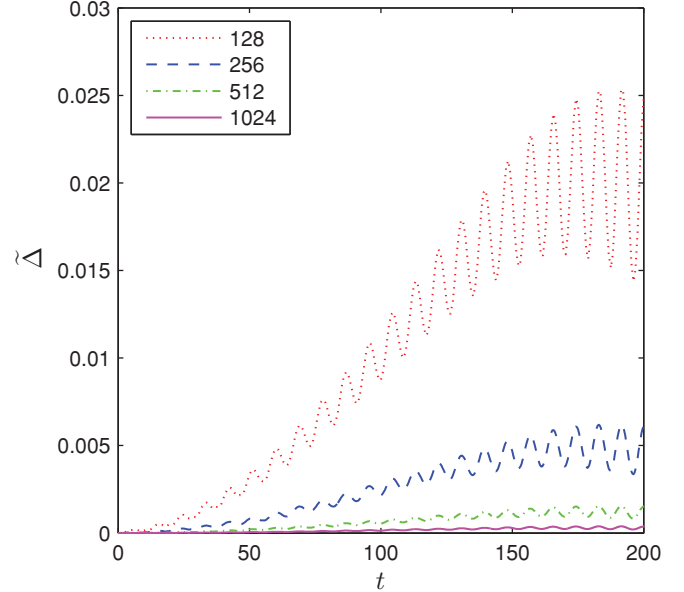


FIG. 2. (Color online) Evolution of the average difference $\tilde{\Delta}$ between the three spreads for a wave packet with initial spread $\Delta_0 = 14$, mass $m = 0.35$, and no potential in a cube with side length $\ell = 100$. The cube was discretized using 128^3 , 256^3 , 512^3 , and 1024^3 points.

refinement. Figure 3 shows that the rescaled spread differences $n^2 \tilde{\Delta}$ for the four different grids agree very closely, confirming that $\tilde{\Delta} = \mathcal{O}(n^{-2})$. We thus obtain second-order convergence toward isotropy, at least as measured by invariance under 90° rotations.

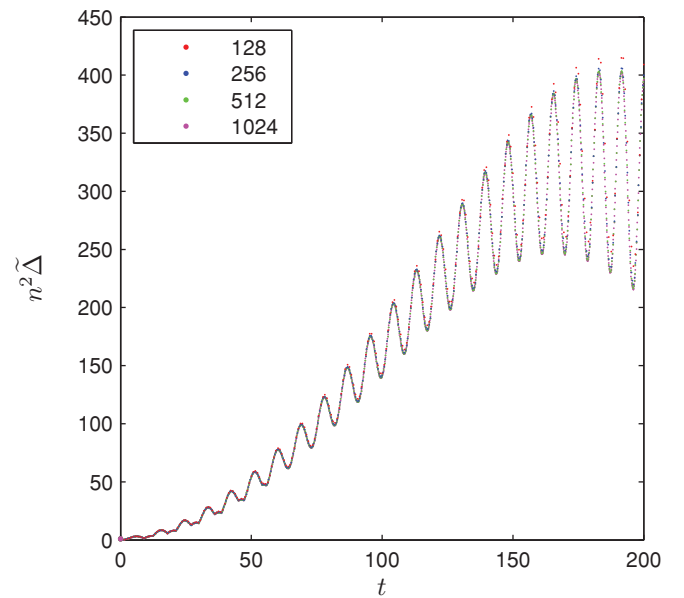


FIG. 3. (Color online) Evolution of $n^2 \tilde{\Delta}$ for a wave packet with initial spread $\Delta_0 = 14$, mass $m = 0.35$, and no potential in a cube with side length $\ell = 100$. The scaled mean anisotropies $n^2 \tilde{\Delta}$ collapse onto a single curve for four different computations using n^3 points with $n = 128, 256, 512, 1024$.

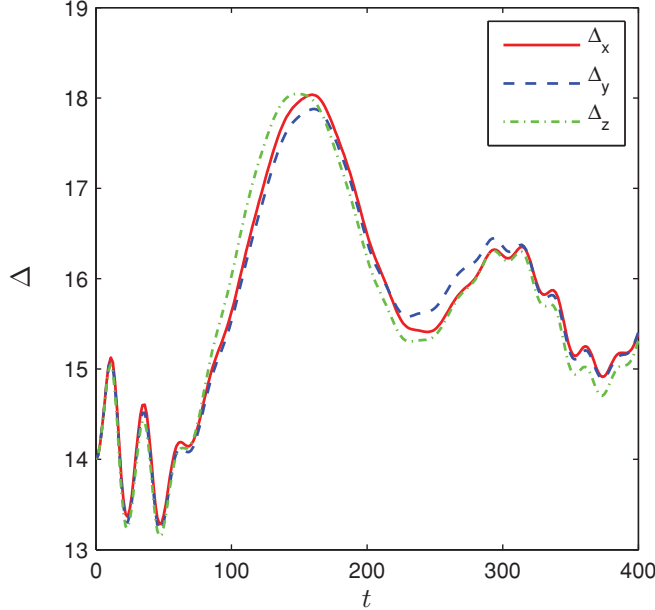


FIG. 4. (Color online) Evolution of the computed spreads Δ_x , Δ_y , Δ_z for a wave packet with initial spread $\Delta_0 = 14$, particle mass $m = 0.1$, potential $\omega_0 = 1/(2m\Delta_0^2)$, in a cube with side length $\ell = 200$ discretized with 128^3 points.

B. Harmonic potential

In this second test case, we consider the Gaussian wave packet of Eq. (24) confined in a spherically symmetric harmonic potential,

$$V(r) = -\frac{1}{2}m\omega_0^2r^2,$$

in our sign convention, where $r^2 = x^2 + y^2 + z^2$, and ω_0 is the frequency associated with harmonic oscillations in this potential. Again, the analytical solution of the Schrödinger equation for this potential is well known, and setting

$$\omega_0 = \frac{1}{2m\Delta_0^2}$$

leads to the initial spread Δ_0 of the wave packet being preserved by subsequent evolution under the Schrödinger equation.

We investigate the ability of the scheme to preserve isotropy of the solution. We set $m = 0.1$ and $\Delta_0 = 14$ thus yielding $\omega_0 = 0.0255$ and hence a period of about $T = 2\pi/\omega_0 \sim 250$ time units based on a box side of length $\ell = 200$ and $c = 1$. As before, we perform simulations with discretization using 128^3 , 256^3 , 512^3 , and 1024^3 points.

In Fig. 4, we show the spreads Δ_x , Δ_y , and Δ_z as functions of time. They are in good agreement with each other, but show large excursions from the value $\Delta = 14$ one would expect them to take if the wave packet evolved under the Schrödinger equation. Figure 5 shows the mean difference $\tilde{\Delta}$ between the three spreads. We observe first-order convergence toward 90° rotational symmetry for $t \lesssim 80$, as confirmed by the rescaled plot of $n\tilde{\Delta}$ in Fig. 6, but no convergence is visible at later times. This appears to be due to the sensitive dependence of the solutions on spatial resolution, as described in Ref. [26].

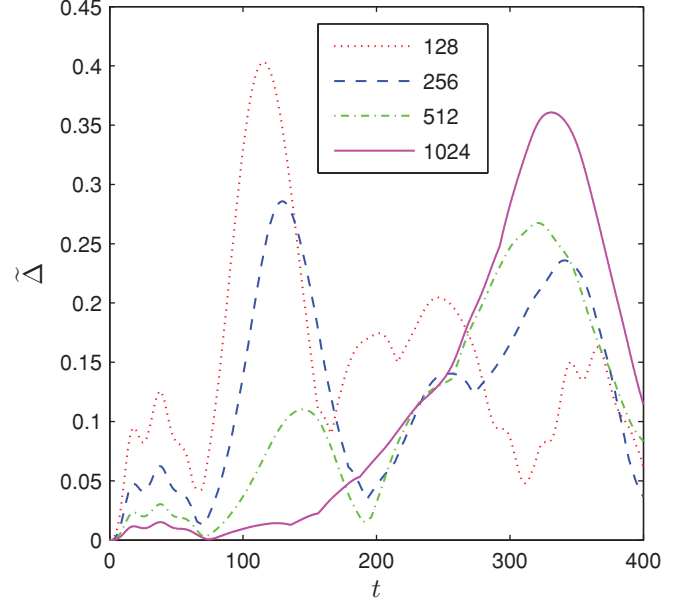


FIG. 5. (Color online) Evolution of $\tilde{\Delta}$ for a wave packet with initial spread $\Delta_0 = 14$, mass $m = 0.1$, potential $\omega_0 = 1/(2m\Delta_0^2)$, in a cube with side length $\ell = 200$. The cube was discretized using 128^3 , 256^3 , 512^3 , and 1024^3 points.

C. Convergence to spherical symmetry

A more demanding test of isotropy is given by testing the convergence of the numerical solutions toward spherical symmetry, rather than just symmetry under 90° rotations. We divide the computational domain up into spherical shells, $r \in [r_i, r_i + \Delta r]$, and perform a least squares fit of $|\phi_1^+|$ to

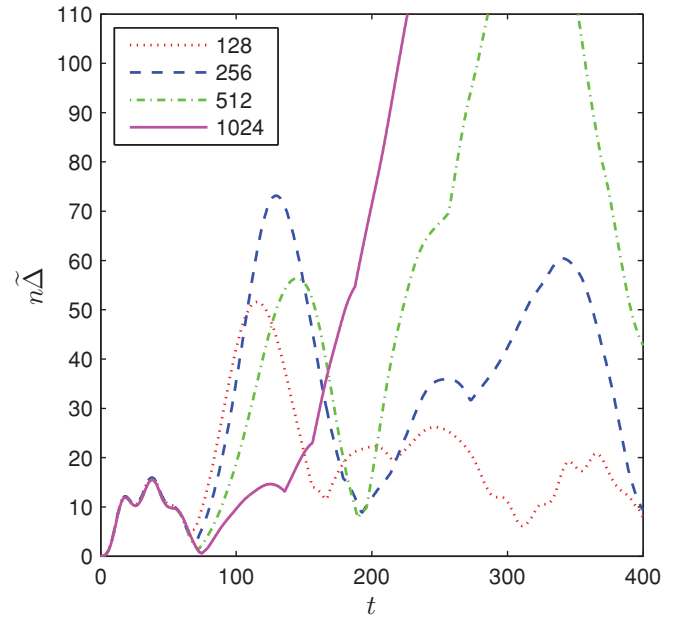


FIG. 6. (Color online) Evolution of $n\tilde{\Delta}$ for a wave packet with initial spread $\Delta_0 = 14$, mass $m = 0.1$, potential $\omega_0 = 1/(2m\Delta_0^2)$, in a cube with side length $\ell = 200$. The cube was discretized using 128^3 , 256^3 , 512^3 , and 1024^3 points. The scaled anisotropies $n\tilde{\Delta}$ collapse into a single curve for $t \lesssim 60$.

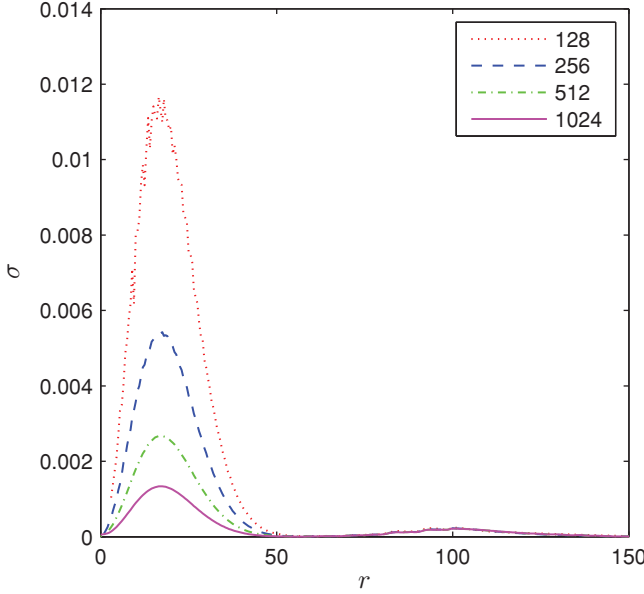


FIG. 7. (Color online) Plot of $\sigma(r)$ at $t = 100$ for $n = 128, 256, 512, 1024$ in a cube of side $\ell = 200$. The feature at $r \approx 100$ is due to coupling with negative energy states that have passed through the periodic boundaries. The 128^3 grid contains too few points to compute σ for $r < 3$.

a linear function $a_i + b_i r$ within each shell. We thus construct a piecewise-linear and spherically symmetric solution by averaging the computed solution over spherical shells. The standard deviation $\sigma(r)$ of the computed $|\phi_1^+|$ away from this spherical average gives a measure of the deviation of the computed solution away from spherical symmetry. Figure 7

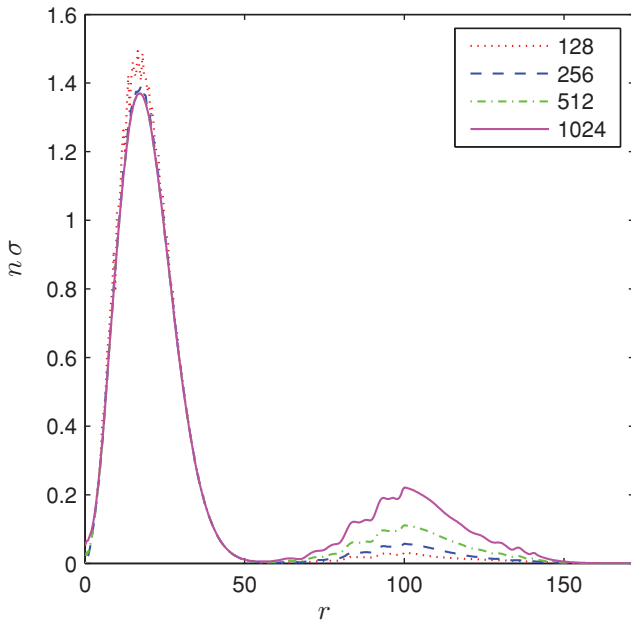


FIG. 8. (Color online) Plot of $n\sigma(r)$ at $t = 100$ for $n = 128, 256, 512, 1024$ confirming first-order convergence to spherical symmetry under grid refinement in the region $r \lesssim 50$. The nonconverging feature centered at $r \approx 100$ is due to coupling with negative energy states that have passed through the periodic boundaries.

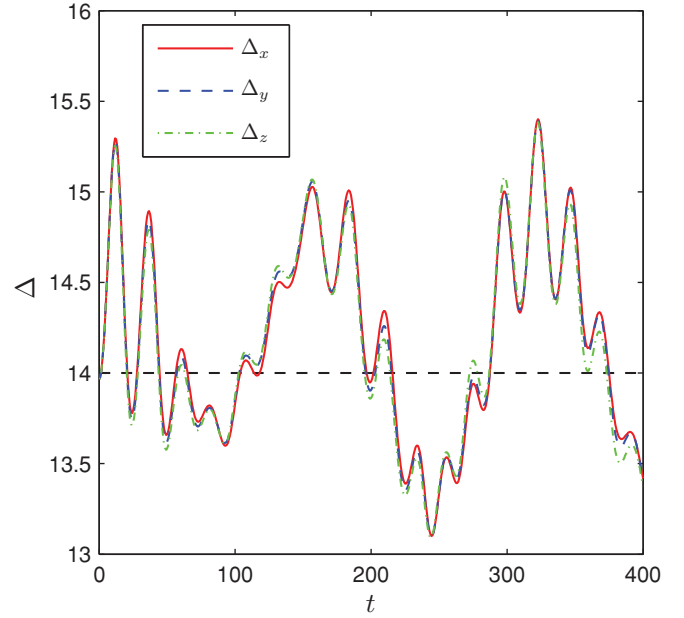


FIG. 9. (Color online) Dispersion of a wave packet with initial spread $\Delta_0 = 14$, particle mass $m = 0.1$, potential $\omega_0 = 1/(2m\Delta_0^2)$, in a cube with side length $\ell = 100$ and a computational grid with 128^3 points. Computed spreads $\Delta_x, \Delta_y, \Delta_z$.

shows the function $\sigma(r)$ for the computed solutions at $t = 100$ and a bin size $\Delta r = 1$. The numerical solutions appear to converge toward spherical symmetry in the region $r \lesssim 50$. The feature near $r = 100$ is due to negative energy states being drawn toward the periodic boundaries of the cube by the potential. (A scalar potential that is confining for positive energy states is deconfining for negative energy states, and

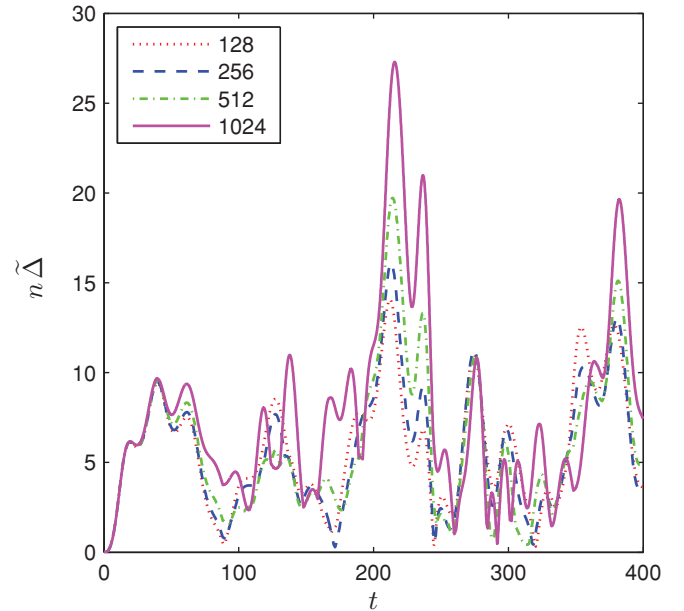


FIG. 10. (Color online) Evolution of $n\tilde{\Delta}$ for a wave packet with initial spread $\Delta_0 = 14$, mass $m = 0.1$, potential $\omega_0 = 1/(2m\Delta_0^2)$, in a cube with side length $\ell = 100$. The computational grids contained n^3 points for $n = 128, 256, 512, 1024$.

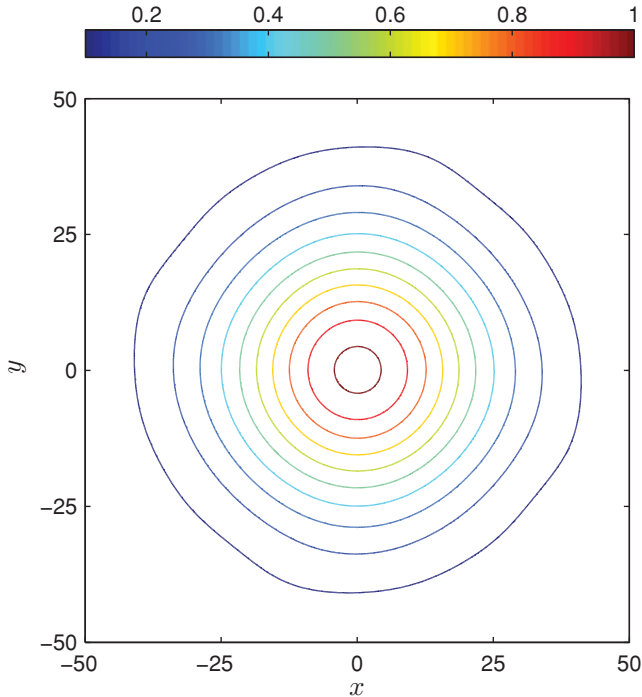


FIG. 11. (Color online) Contours of $|\phi_1^+(x, y, 0)|$ on the plane $z = 0$ from a 512^3 simulation in a cube of side length $\ell = 100$ (values increase from outer circles to inner circles). The contours are noticeably distorted away from circular symmetry by the boundaries of the cube.

vice versa.) This part of the solution is thus not expected to demonstrate spherical symmetry, but first-order convergence toward spherical symmetry of the solution in $r \lesssim 50$ is confirmed by the plot of $n\sigma(r)$ in Fig. 8.

D. Effect of a smaller box

Much better convergence of the three spreads Δ_x , Δ_y , and Δ_z is observed in a smaller box of side $\ell = 100$. Figure 9 shows that the three spreads remain in close agreement from $t = 0$ to $t = 400$, and oscillate around the initial value $\Delta_0 = 14$. The plots of $n\tilde{\Delta}$ in Fig. 10 demonstrate first-order convergence toward 90° rotational symmetry for $t \lesssim 50$. For later times the convergence appears closer to $\tilde{\Delta} = \mathcal{O}(n^{-1/2})$ rather than

$\tilde{\Delta} = \mathcal{O}(n^{-1})$. However, the solution in this smaller box is noticeably distorted away from spherical symmetry by the effects of the boundaries, as shown by the contour plot of $|\phi_1^+|$ on the plane $z = 0$ in Fig. 11, and thus shows no convergence to spherical symmetry under grid refinement.

VI. CONCLUSIONS

The Dirac equation has many structural similarities with the discrete Boltzmann equation that underlies the lattice Boltzmann approach to simulating hydrodynamics. However, it is not possible to discretize the three-dimensional Dirac equation by integration along characteristic curves, as in the derivation of lattice Boltzmann schemes for hydrodynamics. The characteristics of the Dirac equation are not curves but light cones, three-dimensional surfaces in space-time. Instead, we employ operator splitting to separate the solution of the three-dimensional Dirac equation into three one-dimensional steps. Each step involves derivatives with respect to only one spatial coordinate, so each step may be discretized using the one-dimensional quantum lattice Boltzmann scheme. However, within each step the wave function must be transformed into characteristic variables by rotating it using one of the X , Y , Z matrices, evolved using the one-dimensional scheme, then rotated back to its original form ready for the next step. These rotations were applied in the incorrect order in the previous formulation of the quantum lattice Boltzmann scheme [6]. This led to a severe lack of isotropy in the numerical results, as shown by differences in the values of the three spreads Δ_x , Δ_y , Δ_z that persisted under grid refinement [8]. In this paper we have shown that the corrected scheme recovers isotropy to within a discretization error that typically scales linearly (or better) with the grid resolution. In other words, we have shown first-order convergence toward isotropy, at least for times too short to allow interaction with the boundary, and thus established the viability of the quantum lattice Boltzmann approach in three spatial dimensions.

ACKNOWLEDGMENTS

P.J.D.'s and D.L.'s research was supported by the UK Engineering and Physical Sciences Research Council, Grant No. EP/E054625/1. Some of the computations made use of the facilities of the Oxford Supercomputing Centre.

-
- [1] S. Chen and G. D. Doolen, *Annu. Rev. Fluid Mech.* **30**, 329 (1998).
 - [2] S. Succi, *The Lattice Boltzmann Equation: For Fluid Dynamics and Beyond* (Oxford University Press, Oxford, 2001).
 - [3] D. Yu, R. Mei, L.-S. Luo, and W. Shyy, *Progress Aerospace Sci.* **39**, 329 (2003).
 - [4] C. K. Aidun and J. R. Clausen, *Annu. Rev. Fluid Mech.* **42**, 439 (2010).
 - [5] R. Benzi, S. Succi, and M. Vergassola, *Phys. Rep.* **222**, 145 (1992).
 - [6] S. Succi and R. Benzi, *Physica D* **69**, 327 (1993).
 - [7] S. Succi, *Phys. Rev. E* **53**, 1969 (1996).
 - [8] S. Palpacelli and S. Succi, *Phys. Rev. E* **75**, 066704 (2007).
 - [9] S. Palpacelli and S. Succi, *Comput. Phys. Commun.* **4**, 980 (2008).
 - [10] V. B. Berestetskii, E. M. Lifshitz, and L. P. Pitaevskii, *Quantum Electrodynamics* (Butterworth-Heinemann, Oxford, 1982), 2nd ed.
 - [11] K. O. Friedrichs, *Commun. Pure Appl. Math.* **7**, 345 (1954).
 - [12] S. Benzoni-Gavage and D. Serre, *Multi-Dimensional Hyperbolic Partial Differential Equations: First Order Systems and Applications* (Oxford University Press, Oxford, 2007).
 - [13] G. B. Whitham, *Linear and Nonlinear Waves* (Wiley Interscience, New York, 1974).

- [14] I. Bialynicki-Birula, *Phys. Rev. D* **49**, 6920 (1994).
- [15] D. A. Meyer, *J. Stat. Phys.* **85**, 551 (1996).
- [16] D. A. Meyer, *Phys. Rev. E* **55**, 5261 (1997).
- [17] B. M. Boghosian and W. Taylor, *Physica D* **120**, 30 (1998).
- [18] B. M. Boghosian and W. Taylor, *Phys. Rev. E* **57**, 54 (1998).
- [19] L. Vahala, G. Vahala, and J. Yepez, *Phys. Lett. A* **306**, 227 (2003).
- [20] R. P. Feynman and A. R. Hibbs, *Quantum Mechanics and Path Integrals* (McGraw-Hill, New York, 1965).
- [21] U. Frisch, B. Hasslacher, and Y. Pomeau, *Phys. Rev. Lett.* **56**, 1505 (1986).
- [22] S. Wolfram, *J. Stat. Phys.* **45**, 471 (1986).
- [23] G. 't Hooft, *J. Stat. Phys.* **53**, 323 (1988).
- [24] G. 't Hooft, *Int. J. Mod. Phys. A* **25**, 4385 (2010).
- [25] S. Palpacelli, S. Succi, and R. Spigler, *Phys. Rev. E* **76**, 036712 (2007).
- [26] D. Lapitski and P. J. Dellar, *Philos. Trans. R. Soc. London, Ser. A*, doi:10.1098/rsta.2011.0017.
- [27] L. Haddad and L. Carr, *Physica D* **238**, 1413 (2009).
- [28] K. S. Novoselov, A. K. Geim, S. V. Morozov, D. Jiang, M. I. Katsnelson, I. V. Grigorieva, S. V. Dubonos, and A. A. Firsov, *Nature (London)* **438**, 197 (2005).
- [29] Y. Zhang, Y.-W. Tan, H. L. Stormer, and P. Kim, *Nature (London)* **438**, 201 (2005).
- [30] M. I. Katsnelson, K. S. Novoselov, and A. K. Geim, *Nat. Phys.* **2**, 620 (2006).
- [31] A. H. Castro Neto, F. Guinea, N. M. R. Peres, K. S. Novoselov, and A. K. Geim, *Rev. Mod. Phys.* **81**, 109 (2009).
- [32] G. R. McNamara and G. Zanetti, *Phys. Rev. Lett.* **61**, 2332 (1988).
- [33] F. J. Higuera and J. Jiménez, *Europhys. Lett.* **9**, 663 (1989).
- [34] F. J. Higuera, S. Succi, and R. Benzi, *Europhys. Lett.* **9**, 345 (1989).
- [35] D. d'Humières, in *Rarefied Gas Dynamics: Theory and Simulations*, edited by B. D. Shizgal and D. P. Weaver, *Prog. Astronaut. Aeronaut.*, vol. 159 (AIAA, Washington, D.C., 1994), pp. 450–458.
- [36] P. Lallemand and L.-S. Luo, *Phys. Rev. E* **61**, 6546 (2000).
- [37] P. J. Dellar, *J. Comput. Phys.* **190**, 351 (2003).
- [38] X. He, S. Chen, and G. D. Doolen, *J. Comput. Phys.* **146**, 282 (1998).
- [39] X. He and L.-S. Luo, *Phys. Rev. E* **55**, R6333 (1997).
- [40] X. He and L.-S. Luo, *Phys. Rev. E* **56**, 6811 (1997).
- [41] J. P. Boyd, *Chebyshev and Fourier Spectral Methods*, 2nd ed. (Dover, New York, 2000).